

**Particle Habit In Tropical Ice Clouds During CRYSTAL-FACE: Comparison of Two  
Remote Sensing Techniques With In Situ Observations.**

H. Chepfer<sup>1</sup>, V. Noel<sup>2</sup>, P. Minnis<sup>3</sup>, D. Baumgardner<sup>4</sup>, L. Nguyen<sup>3</sup>, G. Raga<sup>4</sup>, M.J. McGill<sup>5</sup>, P.  
Yang<sup>6</sup>

<sup>1</sup>LMD/IPSL, Palaiseau, France.

<sup>2</sup>AS&M, Hampton, VA, USA

<sup>3</sup>NASA/LaRC, Hampton, VA, USA

<sup>4</sup>Universidad Nacional Autónoma de México, Mexico.

<sup>5</sup>NASA/GSFC, Washington DC, USA

<sup>6</sup>Department of Atmospheric Sciences, Texas A&M University, College Station, Texas, USA

Submitted to JGR

September 2004

**Corresponding author :**

Hélène Chepfer

LMD/IPSL

Ecole Polytechnique

91128 Palaiseau Cedex

France

Tel : 33 1 69 33 36 06

Fax : 33 1 69 33 30 05

E-mail : chepfer@lmd.polytechnique.fr

**Abstract.**

Ice crystal shapes in tropical ice clouds are estimated with two different remote sensing methods and compared with measurements from an in-situ cloud aerosol spectrometer (CAS) during the Cirrus Regional Study of Tropical Anvils and Cirrus Layers - Florida Area Cirrus Experiment (CRYSTAL-FACE) campaign conducted in Florida during July 2002. The remote sensing techniques use dual-satellite reflectances and lidar linear depolarization rate. The ice crystal shape is derived from CAS measurements of forward and backscattered light from individual particles in the size range from 1 – 45  $\mu\text{m}$ . The remote sensing and in situ retrievals are based on ice crystal optical models, which incorporate the scattering phase functions integrated over the collection angles used by the CAS, the view angles from dual-satellites retrievals, and the complete scattering matrix for lidar. Due to the space and time collocation constraint between in situ and remote sensing techniques, data from only one day are used to evaluate the dual-satellite technique (July 11) and from three days for the lidar (July 23, 26, and 29). Data from July 23 and 29 are also used to compare the two remote sensing techniques. In total, 40 shape retrievals were obtained for 20 different cloud areas, allowing paired comparisons of the methods. The results show consistent particle shapes for half of the cloud areas studied. The discrepancies for the other cases can be explained by insufficient spatial-temporal collocations of the data or limitations of the CAS that constrain its range to particles  $< 45 \mu\text{m}$ , whereas the remote sensing techniques are influenced by particles outside the size range of the CAS.

## 1. Introduction

Ice clouds play a major role in the atmospheric energy balance (Liou 1986, Stephens 1991) through their albedo and greenhouse effects. The determination of ice cloud microphysical and macrophysical properties from in situ and remote sensing observations remains a challenging task. Ice cloud microphysical properties such as particle size, shape and orientation vary in space and time yet must be accurately characterized since they influence the cloud interactions with radiation. In the shortwave radiative domain, the relative fraction of light scattered in the upward and downward hemispheres is sensitive to the particle shape. For example, simple plane-parallel radiative transfer computations demonstrate that cloud albedo can be modified as much as 20% at constant ice water content for the same cloud composed of various particle habits. Improving our knowledge of particle habits in various locations and times is the goal of numerous studies using in situ observations collected during several intensive field experiments (e.g., *Randall et al. 1996*, *Raschke et al. 1998*, *McFarquar and Heymsfield 1996*, *Toon and Miake-Lye 1998*). The results of these in situ analyses illustrate the large variability of particle shape (e.g., *Heymsfield 1975*, *Heymsfield et al. 1984*, *Heymsfield 1993*, *Francis et al. 1994*), and highlight potential links between the crystal habit and the latitude, and atmospheric temperature and humidity. Those studies also show that the particle microphysical properties, if averaged over the entire globe, are probably not particularly relevant to understanding the physical processes underlying crystal formation at specific latitudes under different dynamical environments.

Some remote sensing methods have been developed to detect signatures of variations in ice cloud microphysical properties, so that global satellite coverage can be used to develop a better description of those properties at various latitudes and time periods. These methods start with estimates of the ice crystal sizes (Inoue 1985, Minnis et al. 1993, Minnis et al. 1998, King et al. 2003, Platnick et al. 2003) using both geostationary and low orbiting satellites. More recently,

active remote sensing techniques have been developed to utilize ground based active observations (Intrieri et al. 1993, Mace et al. 2002). More recent efforts have been directed towards deriving ice crystal shape from remote sensors, or at least estimating the asymmetry factor that is the link between the crystal habit and its radiative impact on the albedo. The methods developed to retrieve information on the crystal shape (Baran et al. 1999, Chepfer et al. 1998, Noel et al. 2001, Masuda et al. 2002, Chepfer et al. 2002) usually utilize visible wavelengths because the signature of variations in crystal habit is dominant at those wavelengths in comparison with the infrared or millimeter domain. Some techniques use bidirectional reflectance observations to detect different signatures linked to the scattering phase function depending on the crystal shape, or observations of the state of polarization of light scattered by the particle, another parameter strongly dependent on the crystal shape.

The goal of this paper is to compare the shapes of crystals in tropical clouds derived from satellites and lidar to in situ measurements in order to assess the capability of remote sensors to resolve crystal shapes. The first technique (Chepfer et al. 2002) uses dual satellite observations and takes advantage of bidirectional reflectance signatures. The second method (Noel et al. 2001, Noel et al. 2004) is based on the depolarization ratio observed in lidar backscattering. The in-situ retrieval takes advantage of bidirectional light scattering measurements of single particles made with the Cloud and Aerosol Spectrometer (CAS, see Baumgardner et al. 2004). The two remote sensing technique are applied to small data sets collocated in space and time with in situ observations taken during the Cirrus Regional Study of Tropical Anvils and Cirrus Layers - Florida Area Cirrus Experiment (CRYSTAL-FACE) campaign (Jensen et al. 2004) conducted between July 1 and 30, 2002 over Florida and the Gulf of Mexico. In the future, the dual satellite technique can be applied to collocated observations by geostationary and low-orbiting satellites, whereas the lidar technique can be applied to space borne lidar with polarization capabilities

(Winker et al. 2002) leading to global maps of the particle shape and visible wavelength asymmetry factors. This paper provides the first in a series of validation efforts for these two potentially valuable remote sensing methods.

## 2. Observations

The current data set was collected in tropical ice clouds during the CRYSTAL-FACE campaign in July 2002. The cloud cases studied examined here correspond to times when the satellite and/or ER2 remote sensing observations were collocated in the same cloud area to within 24 km of the WB-57F aircraft. The matching requires that the WB-57F flies through cirrus clouds during the NOAA-16 or Aqua overpasses and that the scattering angle between the target and the AVHRR or MODIS is sufficiently different from that between the target and the Geostationary Operational Environmental Satellite (GOES) imager

### a. Dual satellite data

In the dual-satellite technique, a given cloud area is observed by two satellites from two directions. For both satellites, the radiances are measured at 650 nm, collocated in space and time (less than 15 min difference) and inter-calibrated as in Minnis et al. (2002). For CRYSTAL-FACE (CF), the two satellite sensors are the Eighth Geostationary Operational Environmental Satellite (*G8*) imager and the *NOAA-16* (N16) Advanced Very High Resolution Radiometer (AVHRR) or the *GOES-8* (G8) imager and *Aqua* Moderate Resolution Imaging Spectroradiometer (MODIS). During the *NOAA-16* (N16) and *Aqua* overpasses, the solar zenith angle generally varied between 10 and 30°. The cloud areas were observed at scattering angles around 150° and 110°. The WB-57F aircraft, which carries the CAS, passed through cirrus clouds during the July 11 N-16 overpasses and during July 23 and 29 under the ER-2 aircraft which

carried the lidar. A thin cloud was sampled above Florida (**Fig.1a**) during July 11 around 1830 UTC. The mean GOES-8 IR brightness temperatures for three different WB-57F flight segments, designated Z0, Z1, and Z2, are 240K, 223K and 213K, respectively. These segments are considered separately for comparison with the in situ data. On July 23 the WB-57F sampled a thick ice cloud above Florida just before 2000 UTC. Two different cloud segments with IR temperatures lower than 222 K were collocated with the ER-2 flight track (Fig. 1b) and used for comparisons with lidar retrievals. At 1920 UTC, 29 July (not shown), the WB-57F flew through a thick cloud along the ER-2 flight track above the Gulf of Mexico off the Florida peninsula. The satellite viewing directions for each case study are given in **Table 1**. The satellite data were averaged along the WB-57F and the ER-2 flight tracks in three different super pixels covering areas with boxes of 3x3 km, 18x18km and 36x36km.

#### b. Lidar airborne data

The Cloud Profiler Lidar (CPL, McGill et al. 2004) is an airborne Nd-Yag lidar with polarization capabilities that was flying onboard the ER-2 aircraft during the CF mission. This study uses the lidar linear depolarisation ratio ( $\Delta p$ ) determined at 1024 nm. The vertical and temporal resolutions are 30 m and 10s, respectively. The laser shot on the cloud has a typical diameter of 1 m varying with the ER-2 distance to the cloud.

**Figure 2** shows the cloud sequences as observed by the CPL in polarization, and the collocated WB57 flight track within the cloud. Data from 23, 26, and 29 July are compared with the CAS retrievals. Eight, three, and one flight segments were selected for 23, 26<sup>th</sup> and 29 July, respectively. The time difference between the ER-2 and the WB-57F is less than 10 min, and the space collocation better than 2 km. The lidar retrievals are extracted for the portion of the cloud at the altitude of the WB57. Three complementary cloud segments taken from 23 and 29 July

data were selected for comparison with the dual satellite retrievals. The different segments considered are summarized in Table 1.

c. In Situ data

The CAS (Baumgardner et al. 2002) observes particles with diameters ranging between 1 and 45  $\mu\text{m}$ . It measures forward and backward light intensity scattered by individual particles that pass through a laser ( $\lambda = 680 \text{ nm}$ ). The forward cone of light is between  $4^\circ$  and  $12^\circ$ , and the backscattering cone between  $168^\circ$  and  $176^\circ$ . The CAS was mounted on the left wing of the NASA WB-57F aircraft during CRYSTAL-FACE. Eighteen CAS segments, collocated in space and time with remote sensing observations, are used in the current study (**Table 1**).

### 3. Retrieval methods

a. Ice crystal optical properties

The remote sensing and in situ methods interpret measurements of light scattered in the visible domain using theoretical ice crystal optical properties. In this wavelength domain, pure ice scatters light conservatively. When the particle size is larger than 10  $\mu\text{m}$ , the theoretical properties (including the scattering phase function and the complete scattering matrix) are computed in the framework of geometric optics approximation enhanced with Fraunhofer diffraction. Geometric optics is independent of the particle size, unlike Fraunhofer diffraction. As a consequence, when the scattering angle is larger than  $3^\circ$ , where the main diffraction peak is negligible, the scattering phase function (and scattering matrix) is less dependent on particle size. However, the secondary diffraction peaks still have some influence but at a smaller level. The in situ and two remote sensing methods use the phase function (or scattering matrix) at various

scattering angles ranging between  $4^\circ$  and  $180^\circ$ ; hence, the information obtained with those methods is mainly a signature of the particle shape when the size of the particles under study exceeds  $10\text{ }\mu\text{m}$ . During the CF campaign, a large quantity of particles smaller than  $10\text{ }\mu\text{m}$  were observed, so optical properties computed with the finite difference time domain method, which is adapted for small particles, are also considered in the current study. The phase function obtained with this computation method is strongly sensitive to the particle size in small scattering angles but is still mainly sensitive to crystal shape at large angles. Hence, the in situ retrieval, which uses observations in both scattering angle ranges ( $4\text{-}12^\circ$  and  $168\text{-}176^\circ$ ), will be sensitive to both particle size and shape, whereas the retrievals based on observations at large scattering angles ( $>110^\circ$  for satellites, around  $180^\circ$  for lidar) are primarily sensitive to particle shape only.

Twenty state-of-the-art ice crystal models in the visible domain are summarized in **Table 2**. They contain simple mono-modal ice crystals and more complex ones composed of mixed of particles. The detailed algorithms for computing the single-scattering properties of these particles can be found in the literature (e.g., Wendling et al. 1979, Takano and Liou 1989, Macke et al. 1996, Yang and Liou 1996, 1998, Noel et al. 2001). For the MODIS models in Table 2, the population of ice crystals consists of various ice crystal habitats with certain percentages (Baum et al., 2001; King et al., 2004). Note that the CERES (Minnis et al. 1998) and MODIS models correspond to different particle size distributions. Within these mixed distributions, the smallest ones (CERES-cont and MODIS-1) include particles smaller than  $10\text{ }\mu\text{m}$ . According to in situ observations (e.g., Auer and Veal, 1970), the dominant aspect ratio of small pristine ice crystals is approximately one (i.e., the compact ice crystals). Droxtals have been observed within ice fog and ice clouds (Thuman and Robinson, 1954; Zhang et al., 2003). This type of ice crystals has the basic hexagonal structure. However, a droxtal ice crystal has 20 faces instead of a geometry of a well-



developed hexagonal column to plate. In this study, we consider four mono-crystal models corresponding to particles smaller than 10  $\mu\text{m}$ : Compact-C and Columns-B (Takano and Liou 1989), droxtal-4  $\mu\text{m}$  and droxtal-6  $\mu\text{m}$  (Yang et al. 2004, Zhang et al. 2004). Two spherical crystal models (diameter 12  $\mu\text{m}$  and 6  $\mu\text{m}$ ) computed with Mie theory are also considered as a reference. Figure 3 illustrates the variation in the scattering phase function for four different crystals types.

b. The dual satellite retrieval method.

This method simulates radiance at the top of the atmosphere in the viewing directions of the two satellites for clouds composed of the different particles types summarized in **Table 2**, and for various optical depths ranging between 1 and 100, using an adding-doubling radiative transfer code (De Haan et al. 1986). The theoretical ratio,  $R_{\text{sat\_t}}$ , between the radiance in the two viewing directions is computed. Because of the difference in the phase function between the two directions around scattering angles of  $150^\circ$  and  $110^\circ$  the order of magnitude of  $R_{\text{sat-t}}$  ranges between 0.8 and 1.2 depending on the viewing directions. This simulated ratio can be directly compared to the one measured with the two satellites in order to select the phase functions consistent with the dual-satellite observations. All the models listed in Table 2 can be tested because this method requires only the scattering phase function for the radiative transfer calculations.

This method has been previously applied to 28 ice cloud cases studied over North America and the Atlantic Ocean (Chepfer et al. 2002) to observe variation of the ice particle shapes, but has never been validated against in-situ observations.

c. The lidar depolarization retrieval method.

This method simulates the linear lidar depolarisation ( $\Delta p$ ) ratio for the different particle shapes summarized in **Table 2** to account for the multiple scattering at cloud optical thickness ranging between 0 and 3. The lidar can not penetrate larger optical depths. The simulated  $\Delta p$  is compared to the measured value to select the particle model that best fits the observations. This method can be used to discriminate between classes of particle that correspond to 4 different shape ratios: class 1 ( $Q < 0.05$ ), class 2 ( $0.05 < Q < 0.7$ ), class 3 ( $0.7 < Q < 1.05$ ), class 4 ( $Q > 1.05$ ). These are associated with different asymmetry factors in the visible domain. Class 1 represents spherical particles or very thin plates, whereas the other classes are clearly identified as non-spherical particles. This method gives access to the vertical variability of the particle shape within the cloud, as it can be applied to each level detected by the lidar between the cloud top and an optical depth of 3. The number of particle shapes that can be tested is low because the theoretical computation of the scattering matrix in the backscattering direction ( $180^\circ$ ) has to be carefully treated and few models currently have a good treatment of the scattering matrix in this particular direction (Table 2).

This method has been previously applied to 15 mid-latitude ice cloud cases observed with a ground-based lidar (Noel et al. 2002) at the SIRTa site in Palaiseau, France (Haeffelin et al., 2004). Moreover, it has been applied to tropical clouds and compared to in-situ Cloud Particle Imager (CPI) results during CF (Noel et al. 2004), showing a good agreement between remote sensing and in-situ retrieval for large particles.

d. The CAS retrieval method

The method consists of computing the theoretical ratio between the intensity scattered in the forward ( $4^\circ$  -  $12^\circ$ ) and backward ( $168^\circ$  -  $176^\circ$ ) directions for the different particle models summarized in **Table 2**. This theoretical ratio, ranging between 2.5 and 183, is directly compared to the measured one in order to select the most closely associated ice crystal model. All the models shown in Table 2 can be tested, as this method requires only the scattering phase function. This technique gives direct information useful for constraining the crystal model, but it is valid only for particles with sizes ranging between 1 and 45  $\mu\text{m}$ . The CAS method has been applied to the complete CF data set composed of 10 flights of the WB-57F aircraft (Baumgardner et al. 2004), showing that in the size range of the CAS, droxtal mixtures of bullet rosettes, hollow columns and plates (MODIS-rough model) are dominant but 10% of particles correspond to small columns. This retrieval method has not yet been compared to other in situ or remote sensing retrievals of particle shapes.

## 4. Results

### a. Dual satellites results

*11 July Case* : The dual-satellite method was applied to a cloud area observed above Florida during 11 July. This cloud is thin and heterogeneous. The satellite viewing angles vary by only  $\pm 0.5^\circ$  and the time difference between *GOES-8* and *NOAA-16* is five minutes. The cloud is separated in four areas (Z0 - Z3), the first one with temperatures ranging between 225 and 222 K, and the others with mean temperatures of 213 K. The comparisons between the simulated and observed radiances are plotted in **Figures 4a** and 4b for Z1 and Z3 : the theoretical ratio between the *GOES-8* and *NOAA-16* radiances is shown as a function of the radiance observed in the *GOES-8* direction. Each data point corresponds to  $36 \times 36 \text{ km}^2$ . The column model is the most

appropriate to explain the measurements in area Z1, similar behaviors are obtained in Z0 and Z2 (not shown). Figure 4b shows that the last area (Z3) is more consistent with the spherical model.

23 July : The time difference between *GOES-8* and *NOAA-16* is 15 min and two cloud areas are examined: Z1 with  $T = 215\text{K}$  and Z2 with  $T = 220\text{K}$ . Figure 4c illustrates the comparison of observations and simulations for the first area, with satellite data averaged over 3 km, 18 km and 36 km along the ER-2 flight track. This figure clearly illustrates the need to average the data over 36 km for a reasonable comparison due to the time difference between the two satellites. This behavior is confirmed by the other case studied (not shown) and all the satellite retrievals use the 36x36 km satellite observations. For Z1, the Column model is best suited to explain the observations, whereas for Z2 the spherical model is more appropriate.

29 July : The time difference between *GOES-8* and *Aqua* is 10 min and  $T = 219\text{K}$ . Figure 4d shows that theoretical ratios corresponding to a mixture of plates, bullet-rosettes and hollow columns are most consistent with the satellite observations.

#### b. Lidar results

The lidar shape ratio retrievals were performed along the WB-57F flight-track with a collocation of less than 10 min and 2 km. **Figure 4** shows an example of the histograms of shape ratio obtained for the different cloud segments selected for 23 July (Table 1). Segments 1 - 3 are dominated by ice crystals associated with shape ratios less than one while class 4, associated to large shape ratios ( $>1$ ), is observed most often for segments 4-7. The 40% of class 1 in segment 2 can be associated with spherical water particles, frozen droplets, or very thin ice plates with  $Q < 0.05$ . Segments 5, 7 and 8 show a somewhat uniform mix of particles in all four classes. Data from the 26<sup>th</sup> of July (not shown) yield more than 80% spherical or thin plates particles for segment 1, and a predominance of ice crystals having  $Q \geq 1.0$  for segments 2-4. The single

segment taken during 29 July is dominated by a plate-like shape ratio (class 2) that coexists with other particles.

For the 23rd and 29th of July segments, selected for comparisons with satellite retrievals, the lidar retrievals were processed for the complete vertical structure of clouds seen by the lidar in the same latitude / longitude area as considered for the satellite. The data for the 23<sup>rd</sup> of July are separated into two cloud areas. For the first one, the lidar retrieval is dominated by  $Q < 1$ , while lidar data for the second one indicate a mixture of spherical and small shape ratios. The 29 July results are also dominated by particles with shape ratios less than unity mixed with a significant quantity of thin plates or spheres.

### c. CAS results

The comparisons between measured and simulated forward-to-backscattering ratios ( $R_{CAS}$ ) are plotted in **Figure 6** for the four days under study. The horizontal line corresponds to the closest models. All measured values of  $R_{CAS}$  range between 80 and 130, hence the ice crystal models associated with smaller values of  $R_{CAS}$  such as MODIS-1, -2, -3, CERES-Cont, CERES-Nov, CERES-Big, ISCCP, Spheres-6, large monocrystals (columns-a, compacts-a,-b, plates, bullet-rosettes) are not plotted in the figure because they are poor candidates to explain the observations.

The observations can be explained by five different models, four that are associated with very small particles having sizes less than 10  $\mu\text{m}$  (droxtal-4 $\mu\text{m}$ , droxtal-6 $\mu\text{m}$ , Columns-b, Compacts-c), and one (MODIS-rough) that corresponds to larger mean size (30  $\mu\text{m}$ ) containing a mixture of different shapes (bullet-rosettes, plates and hollow columns) having rough surfaces. The spherical models, even if associated with small sizes cannot explain the measurements. For 3 of the 5 days

under study (23, 26 and 29 July) the small simple hexagonal columns model is the best candidate for explaining the observations as  $R_{CAS}$  is ranging between 115 and 123. For 11 July, the measured  $R_{CAS}$  values are highly variable. However, for the measurements that are collocated with satellite observations,  $R_{CAS} = 111$  which is close to the MODIS-rough model value.

## **5. Comparison between remote sensing and in-situ results (Table 3)**

### **a. Comparison between dual satellites and CAS results**

The 11 July satellite and in-situ observations are well correlated in space and time. Of course, the WB-57F flies within the cloud at a constant altitude, whereas satellite observations are sensitive to a vertically integrated thickness of cloud. The in-situ and satellite analyses use different viewing directions but they are based on the same scattering phase function. Under the assumption that the altitude level flown by the aircraft is representative of the vertical depth sounded by the satellite, the results can be compared.

The satellite and in situ retrievals give consistent results for two of the four areas (Z1 and Z2), where the column model is judged most appropriate. The inconsistency between satellite and in situ retrieval for the first area (Z0) can be explained by the fact that the shape retrieved from the in situ data (Figure 6) is strongly variable in time for that day at Z0 time. The satellite retrieval was averaged over  $36 \times 36 \text{ km}^2$  around the WB-57F flight track and cannot capture the smaller scale variability seen in Figure 6 that is associated with a short descent of 1 km within the cloud. For area Z3, the inconsistency can be explained by the time difference between the satellite and in situ retrievals, which reaches a maximum of 20 min.

### **b. Comparison between lidar and CAS results**

Following the lidar, five segments among thirteen are dominated by shape ratios larger than unity (segments 4, 5, 6, 7 of July 23, and segment 4 of July 26) that are associated with hexagonal columns. For those segments, the results are consistent with the  $R_{CAS}$  observations that also indicate small hexagonal columns.

For segment 3 of July 23, the lidar retrieval produces results suggesting the presence of many different particle shapes without clear dominance of any one particle type whereas the CAS gives results ranging between columns and droxtals.

For segments 1 and 2 of July 26 and segment 1 of July 29, the lidar retrieval indicates hexagonal plates (shape ratio lower than 1) or spherical particles, whereas the in situ data correspond to small columns. This discrepancy can be due to the cloud spatial heterogeneities that appear in Figures 2b and 2c. In those areas, the in situ sensor has difficulty retrieving the particle shape because the sensor does not encounter a sufficient quantity of particles. For example, Figure 6 shows that the values of the in situ ratio for those three segments is interpolated (in line) and not retrieved (in dot).

For segment 3 of July 26, the lidar data show a dominance of hexagonal compact (unity shape ratio) whereas the in situ obtains small hexagonal columns. This segment corresponds to a 2-km descent of the WB57 within a thick cloud. As shown in Figure 2b, the lidar depolarization value changes within the cloud along the WB57 trajectory, leading to various particle shapes, producing, in the mean, a dominance of hexagonal compacts. On the contrary, the in situ retrieval is quite constant along this trajectory (Figure 6), explained by the capability of the CAS to observe only particles smaller than 45  $\mu\text{m}$  whereas the lidar retrieval is influenced by larger particles having different shape ratios.

For the last two segments (1 and 2 of July 23), the lidar results give hexagonal plates and spheres whereas the CAS indicates small hexagonal columns. This discrepancy may be due to

both the small time period considered (2 and 4 min respectively, see Table 3) and the cloud spatial heterogeneities in this area (Figure 2a).

c. Comparisons between dual satellites and lidar results

Among the three cloud areas used to compare lidar and satellite results, two give consistent results and one does not. For the 23 July area Z2, the lidar retrieval is dominated by spheres or plate-like particles and the satellite retrieval is close to spheres. For 29 July, the lidar retrieval indicates mostly plates (shape ratio lower than 1), whereas the satellite retrieval is ambiguous with four possible solutions: plates, bullet-rosettes and MODIS-1 and 2 models that consist in a mixed of plates, bullet-rosettes and hollow columns. The inconsistency obtained for area Z1 of July 23 (lidar gives plates whereas satellite gives columns) may be due to the 15-min difference between the two satellite observations that necessitated averaging the data over 36x36 km (Figure 3b) and to the 12 min. time difference between the satellite and lidar observations.

## 6. Discussion and Conclusion

In total, 40 ice crystal shape retrievals have been processed using three different methods, and compared two-by-two leading to 20 intercomparisons: four satellite with in situ, 13 lidar with in situ, and three satellite with lidar. Nine of the comparisons give consistent results, two have mixed lidar retrievals that can not be interpreted for the comparisons, and nine cases give inconsistent results. Those inconsistencies can be partially explained as follows.

- In two cases, the spatial-temporal matching of the data appears to be insufficient: the time difference between the two satellites is large (15 min) and the comparative measurements (one lidar, one in situ), are taken 15 min before or after the two satellite images. The development and dissipation of anvils during CF were generally quite rapid and the



clouds typically advected westward. Thus, the sampled fields can be quite different when the measurements are taken 15-min apart.

- In two cases, the lidar retrievals are applied to a dataset that is too short to be representative in a spatially heterogeneous cloud.
- In one case, the in situ retrieval is performed using data along a descent of the WB-57F within the cloud leading to a large variation in shapes that is smoothed out by the large averaging area of the satellite measurements.
- In one case, the in situ retrieval is along an ascent of the WB-57F within the cloud showing variability with altitude in the lidar retrieval but not in the in situ data. That may be a result of the limited size range of the CAS whereas the lidar retrieval is influenced by all the particles sizes.

Hence, among the 9 cases showing disagreement, 7 are likely due to poor spatial-temporal matching and 2 are a result of the physical limitations of the retrieval method. Moreover, the CAS retrieval gives information on the particle shape for particles smaller than 45  $\mu\text{m}$  only. This is not necessarily a limitation as there are very few in situ methods that provide shape information for these very small particles; however, when large particles are present, the CAS might not provide a representative assessment of the particle shapes for the entire sampling space.

Finally, the results obtained in this study are encouraging as the method of using two remote sensors contains valuable information on the particle shape for ice crystals having sizes smaller than 45  $\mu\text{m}$ . Nevertheless, the use of these methods requires some precautions. The dual satellite method has to be applied only when the satellite time difference is small enough (typically less than 15 min) and averages over several pixels (at least 20 km super pixels) can be computed (i.e., the cloud must be large enough). The lidar retrieval seems to be robust only if

applied to data averaged over several minutes within well-formed clouds without strong spatial inhomogeneities.

The remote sensing and in situ techniques all agree in the rejection of a large fraction of the 20 optical property models considered at the beginning of the study (Table 2) and conclude that for the different cloud cases examined here the columns, bullet-rosettes, spheres, plates, droxtal and mixtures of those (MODIS-rough models) are the best candidates. In this sense the three methods are quite consistent but it does not mean that these shapes are necessarily the dominant ones during C-F. Other studies, each using only one of the current methods on the complete C-F dataset (Baumgardner et al., 2004; Noel et al. 2004), indicate that the shape variability is considerably larger than that found here. Vertically, the cloud particle sizes and shapes within a cirrus or anvil cloud can be highly variable (e.g. Garrett et al. 2004) and were not often sampled by the WB-57F because most of its flight legs were level at very high altitudes and primarily sampled either the tops of the anvils or the very thin cirrus clouds that often formed above the anvil. In those areas, especially in the thin cirrus, small particles dominate the spectrum and may not necessarily represent the vertically integrated microphysical structure of the clouds. Thus, it is surprising that the satellite and in situ data agree as well as they do.

Nevertheless, these results show that the lidar has the potential to give quantitative results about the particle shape (or asymmetry factor) on a systematic basis, thus providing information on the vertical variability of the ice crystal shape within the cloud itself. Progress can be made by including more optical models associated with different shapes and sizes in order to approach more realistic crystal habits (or asymmetry factors) rather than four different large classes. As shown in Table 2, however, the main limitation in this approach comes from the lack of ice crystal models with the complete scattering matrix in the backscattering direction. Even without additional models, the application of the lidar method to the future Cloud-Aerosol Lidar and

Infrared Pathfinder (CALIPSO, see Winker et al. 2002) mission global lidar dataset could provide a rough estimate of the variability of ice crystal shape within the cloud at the different latitudes along the satellite track. Such information would represent a large step beyond our current understanding of crystal habits, even if the data do not correspond to the “real” shape as given by in situ observations.

The dual satellite method contains potentially valuable information to discriminate the scattering phase function in the visible domain that is mainly a signature of the particle shape because of the angles considered. This method has an advantage in that it can be used to test all the optical properties available in the literature since it only requires the scattering phase function. Hence, all 20 models presented in Table 2 were tested and new ones can be included with no limitations as they become available. This method requires good collocation in space and time between the two satellites and a robust treatment of their visible-channel calibrations. On one hand, these two constraints require heavy pre-treatment of the satellite data for extensive applications, but on the other hand this method could be applied to the large existing dataset and comprises the visible-channel data from most operational and research satellite imagers. Analysis of those data would yield valuable new information on the spatial and temporal variability of the particle asymmetry factor. This technique is also ideal for application to data from satellite-borne multi-angle view scanners, like the Multi-angle Imaging SpectroRadiometer (MISR; see Diner et al., 2002), that view a given scene from more than one angle during a given overpass.

In addition to logistical, matching, and calibration concerns, a variety of studies should be performed to better understand the retrievals. The sensitivity of the dual satellite method to vertical variations in ice crystal shape and size should be explored to determine what portion of the cloud is represented by the retrieval. Additional in situ data should be taken using vertical profiles that are coincident with the dual-satellite or MISR overpasses using sensors that cover a

wide range of particle sizes. Expert mission planning is essential for achieving that goal. The additional data would also help unravel the results of the lidar retrieval in order to better define shapes from the depolarization ratios. Coincident datasets from future field missions similar to CRYSTAL-FACE and from *Aqua* and CALIPSO will be essential for enhancing the value of the remote sensing methods examined here.

### ***Acknowledgments***

The authors would like to thanks Y. Takano, K-N Liou, and A. Macke for making available ice crystal optical properties. This research was supported by the NASA Earth Science Enterprise through the CRYSTAL-FACE mission.

### **References**

- Auer, A. H., Jr., and D. L. Veal, The dimension of ice crystals in natural clouds, *J. Atmos. Sci.*, 27, 919-926, 1970.
- Baran A. J., S. J. Brown, J. S. Foot, and D. L. Mitchell, Retrieval of tropical cirrus thermal optical depth, crystal size and shape using a dual view instrument at 3.7  $\mu\text{m}$  and 10.8  $\mu\text{m}$ , *J. Atmos. Sci.*, 52, 4246-4263, 1999.
- Baum, B. A., D. P. Kratz, P. Yang, S.C. Ou, Y. Hu, P. Soulen, and S. C. Tsay, Remote sensing of cloud properties using MODIS airborne simulator imagery during SUCCESS. I. Data and Models. *J. Geophys. Res.*, 105, 11,767-11,780, 2000.
- Baumgardner, D., H. Jonsson, W. Dawson, D. O'Connor and R. Newton, The cloud, aerosol and precipitation spectrometer (CAPS): A new instrument for cloud investigations, *Atmos. Res.*, 59-60, 251-264, 2002.

- Baumgardner D., H. Chepfer, G. Raga , and G.L. Kok, The shapes of very small cirrus particles derived from in situ measurements, submitted to *Geophys. Res. Lett.*, 2004.
- Chepfer, H., G. Brogniez, and Y. Fouquart, Cirrus clouds microphysical properties deduced from POLDER observations, *J. Quant. Spectrosc. Radiat. Transfer*, 60, 375-390, 1998.
- Chepfer H., P. Goloub, J. Riedi, J. De Haan, J. W. Hovenier, and P. H. Flamant, Ice crystal shapes in cirrus clouds derived from POLDER-1/ADEOS-1, *J. Geophys. Res.*, 106, 7955-7966, 2001.
- Chepfer H., P. Minnis, D. Young, L. Nguyen, and R. F. Arduini, Retrieval of cirrus cloud ice crystal shapes using visible reflectances from dual-satellite measurements, *J. Geophys Res*; 107, 2002, 10.1029/2000JD000240.
- De Haan J., P. B. Bosma, and J. W. Hovenier, The adding method for multiple scattering of polarized light. *Astron. Astrophys.*, 183, 371-391, 1986.
- Diner, D. J., J. C. Beckert, G. W. Bothwell, and J. I. Rodriguez, Performance of the MISR instrument during its first 20 months in Earth orbit. *IEEE Trans. Geosci. Remote Sensing*. 40, 1449-1466, 2000.
- Francis P. N., A. Jones, R. W. Saunders, K. P. Shine, A. Slingo, and Z. Sun, An observational and theoretical study of the radiative properties of cirrus: Some results from ICE'89. *Quart. J. Roy. Meteor. Soc.*, 120, 809-848, 1994.
- Garrett, T. J., B. C. Navarro, D. G. Baumgardner, P. T. Bui, H. Gerber, R. L. Hermann, A. J. Heymsfield, E. J. Jensen, P. Lawson, P. Minnis, L. Nguyen, M. Poellot, S. K. Pope, F. P. J. Valero, C. H. Twohy, and E. M. Weinstock, In situ measurements of the microphysical and radiative evolution of a Florida cirrus anvil, Submitted *J. Atmos. Sci.*, 2004.
- Haefelin M., C. Boitel, D. Bouniol, H. Chepfer, M. Chiriaco, A. Delaval, P. Drobinski, C. Goukenleuque, M. Grall, A. Holzic, F. Hourdin, F. Lapouge, A. Mathieu, A. Naud, V. Noel, J.

- Pelon, A. Protat, B. Romand, R. Vautard, SIRTa, a French atmospheric observatory for clouds, aerosols and water vapor, submitted to *Ann. Geophys*, 2004.
- Heymsfield A. J., Cirrus uncinus generating cells and the evolution of cirriform clouds. Part I: Aircraft observations of the growth of the ice phase, *J. Atmos. Sci.*, 32, 799-807, 1975.
- Heymsfield A. J., and C. M. R. Platt, A parameterization of the particle size spectrum of ice clouds in terms of the ambient temperature and the ice water content, *J. Atmos. Sci.*, 41, 846-855, 1984.
- Heymsfield A. J., Microphysical structure of stratiform and cirrus clouds, *Aerosol – cloud – climate interactions*. P. V. Hobbs, Ed, 54, in the International Geophysics Series, 233 pp., 1993.
- Intrieri, J. M., G. Stephens, W. Eberhard and T. Uttal, A method for determining cirrus cloud particle sizes using lidar and radar backscattering techniques, *J. Atmos. Sci.*, 32, 88-99.
- Inoue T., On the temperature and the effective emissivity determination of semi-transparent clouds by bi-spectral measurements in the 10  $\mu\text{m}$  window region, *J. Meteor. Soc. Japan*, 63, 88-98, 1985.
- Jensen, R., D. O’C. Starr, and O. B. Toon, Mission investigates tropical cirrus clouds, *EOS*, 85, 45 & 50, 2004.
- King, M. D., W. P. Menzel, Y. J. Kaufman, D. Tanre, B. C. Gao, S. Platnick, S. A. Ackerman, L. A. Remer, R. Pincus, and P. A. Hubanks, 2003: Cloud and aerosol properties, precipitable water, and profiles of temperature and humidity from MODIS, *IEEE Trans. Geosci. Remote Sens.*, 41, 442-458.
- King, M. D., S. Platnick, P. Yang, G. T. Arnold, M. A. Gray, J. C. Riedi, S. A. Ackerman, and K. N. Liou, Remote sensing of liquid water and ice cloud optical thickness, and effective radius

- in the arctic: Application of air-borne multispectral MAS data. *J. Atmos. and Ocean. Technol.* 21, 857-875, 2004.
- Liou K.N., Review. Influence of cirrus clouds on weather and climate processes: A global perspective, *Mon Wea. Rev.*, 114, 1167-1199, 1986.
- Mace, G. G., A. J. Heymsfield, and M. R. Poellot, On retrieving the microphysical properties of cirrus clouds using the moments of the millimeter-wavelength Doppler spectrum, *J. Geophys. Res.*, 107, 4815-4841, 2002.
- McFarquhar, G. M., and A. J. Heymsfield, Microphysical characteristics of three cirrus anvils sampled during the Central Equatorial Pacific Experiment (CEPEX), *J. Atmos. Sci.*, 52, 2401-2423, 1996.
- Macke, A., J. Mueller, and E. Raschke, Single scattering properties of atmospheric ice crystal, *J. Atmos. Sci.*, 53, 2813-2825, 1996.
- Masuda K., Ishimoto H., Takashima T., Retrieval of cirrus optical thickness and ice-shape information using total and polarized reflectance from satellite measurements, *J. Quant. Spectroscopy Rad. Transf.*, 75, 39-51, 2002.
- McGill, M. J., L. Li, W. D. Hart, G. M. Heymsfield, D. L. Hlavka, P. E. Racette, L. Tian, M. A. Vaughan, and D. M. Winker, Combined lidar-radar remote sensing: Initial results from CRYSTAL-FACE, *J. Geophys. Res.*, 109, doi: 10.1029/2003JD004030, 2004.
- Minnis P., P. W. Heck, and D. F. Young, Inference of cirrus cloud properties from satellite observed visible and infrared radiances. Part II: Verification of theoretical radiative properties, *J. Atmos. Sci.*, 50, 1305-1322, 1993.
- Minnis P., D. P. Garber, D. F. Young, R. F. Arduini, and Y. Takano, Parameterizations of reflectance and effective emittance for satellite remote sensing of cloud properties, *J. Atmos. Sci.*, 55, 3313-3339, 1998.

- Minnis, P., L. Nguyen, D. R. Doelling, D. F. Young, W. F. Miller, and D. P. Kratz, Rapid calibration of operational and research meteorological satellite imagers, Part I: Evaluation of research satellite visible channels as references, *J. Atmos. Oceanic Technol.*, *19*, 1233-1249, 2002.
- Noël V., G. Ledanois, H. Chepfer, P. H. Flamant, Computation of single scattering matrix for non-spherical particles randomly or horizontally oriented in space , *Appl. Opt.*, *40*, 4365-4375, 2001.
- Noel V., H. Chepfer, G. Ledanois, A. Delaval, P.H. Flamant, Classification of effective shape ratios in cirrus clouds based on lidar depolarization ratio, *Appl. Opt.*, *41*, 4245-4257, 2002.
- Noel V., D. M. Winker, M. McGill, P. Lawson, Classification of particle shapes from lidar depolarisation ratios in convective cirrus clouds compared to in-situ observations during CRYSTAL-FACE, submitted to *J. Geophys. Res.*, 2004.
- Platnick, S., M. D. King, S. A. Ackerman, W. P. Menzel, B. A. Baum, J. C. Riedi, and R. A. Frey, The MODIS cloud products: Algorithms and examples from Terra.. *IEEE Trans. Geosci. Remote Sens.*, *41*, 459-473, 2003.
- Randall, D., B. Albrecht, S. Cox, D. Johnson, P. Minnis, W. Rossow, and D. Starr, On FIRE at Ten. *Adv. Geophys.*, *38*, 37-177, 1996.
- Raschke E., P. Flamant, Y. Fouquart, P. Hignett, H. Isaka, P. R. Jonas, H. Sundquist, and P. Wendling, Cloud radiation studies during the European Cloud Radiation Experiment (EUCREX), *Surveys in Geophys.*, *19*, 89-138, 1998.
- Sassen, K., The polarization lidar technique for cloud research: A review and current assessment, *Bull. Am. Meteorol. Soc.*, *72*, 1848-1866, 1991.
- Takano, Y., and K. N Liou, Solar radiative transfer in cirrus clouds. Part I : Single-scattering and optical properties of hexagonal ice crystals, *J. Atmos. Sci.*, *46*, 3-19, 1989.



- Thuman, W. C., and E. Robinson, "Studies of Alaskan ice-fog particles," *J Meteor.* 11, 151-156 (1954)
- Toon, O. B. and R. C. Miake-Lye, Subsonic Aircraft: Contrail and Cloud Effects Special Study (SUCCESS), *Geophys. Res. Let.*, 25, 1109-1112, 1998.
- Yang, P., and K. N. Liou, Geometric-Optics-integral-equation method for light scattering by nonspherical ice crystals, *Appl. Opt.*, 35, 6568-6584, 1996.
- Yang P., and K. N. Liou, Single scattering properties of complex ice crystals in terrestrial atmosphere, *Contrib. Atmos. Phys.*, 71, 223-248, 1998.
- Yang, P., B. A. Baum, A. J. Heymsfield, Y. X. Hu, H.-L. Huang, S.-Chee Tsay, and S. Ackerman, Single-scattering properties of droxtals, *J. Quant. Spectrosc. Radiat. Transfer.* 79-80, 1159-1180, 2003.
- Wendling P., R. Wendling, H. K. Weickmann, Scattering of solar radiation by hexagonal ice crystals, *Appl. Opt.*, 18, 2663-2671, 1979.
- Winker, D. M., J. Pelon and M. P. McCormick, The CALIPSO mission: Spaceborne lidar for observation of aerosols and clouds, *SPIE Asia-Pacific Symposium on Remote Sensing of the Atmosphere, Environment and Space*, Hangzhou, China, 23-27 October, 4893-01, 2002.
- Zhang, Z., P. Yang, G. W. Kattawar, S.-C. Tsay, B. A. Baum, H.-L. Huang, Y. X. Hu, A. J. Heymsfield, and J. Reichardt, Geometric optics solution to light scattering by droxtal ice crystals, *Appl. Opt.* 43, 2490-2499, 2004.

## Tables

**Table 1:** Cases studied.

Date July 2000	Area	UTC	Complementary information	UT
	SATELLITES			IN SITU
11	Z0 25.3 / 81.15	G8-18.33 N16-18.26	$\theta_{s-G8}=11.8^{\circ}$ , $\theta_{v-G8}=30.4^{\circ}$ , $\phi_{v-G8}=91.1^{\circ}$ $\theta_{s-N16}=10.85^{\circ}$ , $\theta_{v-N16}=58.3^{\circ}$ , $\phi_{v-N16}=180^{\circ}$	18.36- 18.40
	Z1 25.85 / 80.95		$\theta_{s-G8}=12.1^{\circ}$ , $\theta_{v-G8}=30.6^{\circ}$ , $\phi_{v-G8}=89.6^{\circ}$ $\theta_{s-N16}=11.2^{\circ}$ , $\theta_{v-N16}=57.2^{\circ}$ , $\phi_{v-N16}=179.4^{\circ}$	18.50- 18.55
	Z2 and Z3 25.9 / 80.85		$\theta_{s-G8}=12.2^{\circ}$ , $\theta_{v-G8}=31^{\circ}$ , $\phi_{v-G8}=87.7^{\circ}$ $\theta_{s-N16}=11.3^{\circ}$ , $\theta_{v-N16}=56.9^{\circ}$ , $\phi_{v-N16}=177.4^{\circ}$	18.62- 18.70
	LIDAR			IN SITU
23	24.42 / 81.02	19.72-19.74	z = 13.18 km 13.18-13.50 14.40 13.20 13.80 14.60 13.50 13.50-12.80	19.72-19.74
	80.95 / 26.62	19.78-19.82		19.78-19.82
	81.27 / 26.02	20.23-20.32		20.23-20.32
	81.15 / 26.22	21.16-21.22		21.16-21.22
	81.44 / 25.75	21.67-21.75		21.67-21.75
	81.70 / 27.00	22.16-22.17		22.16-22.17
	81.56 / 25.57	22.57-22.62		22.57-22.62
	80.85 / 26.70	23.05-23.20		23.05-23.20
26	85.80 / 21.13	17.40-17.43	z = 15.70-15.90 km 15.20-15.70 13.00-14.75 15.20-15.90	17.40-17.43
	83.10 / 15.50	18.28-18.51		18.28-18.51
	83.45 / 16.40	19.01-19.14		19.01-19.14
	83.75 / 17.00	19.16-19.21		19.16-19.21
29	82.63 / 26.65	19.88-19.93	z = 12.5 km	19.88-19.93
	SATELLITE			LIDAR
23	Z1 80.80 / 26.75	G8-19.61 N16-19.43	$\theta_{s-G8}=29.9^{\circ}$ , $\theta_{v-G8}=32^{\circ}$ , $\phi_{v-G8}=96.2^{\circ}$ $\theta_{s-N16}=27.6^{\circ}$ , $\theta_{v-N16}=45^{\circ}$ , $\phi_{v-N16}=1.3^{\circ}$	19.81-19.84
	Z2 80.50 / 27.15		$\theta_{s-G8}=30.2^{\circ}$ , $\theta_{v-G8}=32.4^{\circ}$ , $\phi_{v-G8}=94.9^{\circ}$ $\theta_{s-N16}=27.9^{\circ}$ , $\theta_{v-N16}=46.5^{\circ}$ , $\phi_{v-N16}=2.0^{\circ}$	19.89-19.92
29	Z1 80.80 / 26.75	G8-19.32 Aqua-19.18	$\theta_{s-G8}=24.9^{\circ}$ , $\theta_{v-G8}=32.15^{\circ}$ , $\phi_{v-G8}=92.3^{\circ}$ $\theta_{s-N16}=23^{\circ}$ , $\theta_{v-N16}=42.5^{\circ}$ , $\phi_{v-N16}=8.8^{\circ}$	19.18-19.22

**Table 2:** Ice crystal models.  $Q_{eq}$  is the mean equivalent shape ratio (length divided by diameter),  $g$  the asymmetry factor,  $D$  the particle diameter in  $\mu\text{m}$ . The complete scattering matrix in backscattering  $M(180)$  is carefully computed (y) or not (n).

Name	Crystal shapes	$Q_{eq}$	$g$	$D$	$M(180)$	$R_{CAS}$
COL-a	Hexagonal columns	2.5	.80	40	y	4
COL-b	Hexagonal columns	2	0.81	7.5	n	117
COMPa	Hexagonal compacts	1	.70	40	n	5
COMPb	Hexagonal compacts	1	0.74	100	y	2.5
COMPc	Hexagonal compacts	1	0.76	5	n	84
PL1a	Hexagonal plates	0.05	.85	40	n	25
PL1b	Hexagonal plates	0.05	0.90	100	y	11
PL2	Hexagonal plates	0.7	0.74	100	y	3
BR	Bullet rosettes	1	.83	87	n	18
CERES-Big	Hexagonal compacts +columns	>1	.85	135	n	6
CERES-Nov	Hexagonal compacts +columns	>1	.82	75	n	7
CERES-Cont	Hexagonal compacts +columns	>1	.77	18	n	29
MODIS-1	Bullet-rosettes +plates+hollow columns+aggregates	-	.75	9	n	39
MODIS-2	Bullet-rosettes +plates+hollow columns+aggregates	-	.80	33	n	36
MODIS-3	Bullet-rosettes +plates+hollow columns+aggregates	-	.84	79	n	37
MODIS-rough	Bullet-rosettes +plates+hollow columns+aggregates	-		30	n	108
ISCCP	Polycrystals	1	0.70	60	n	66
Droxtal_a	Droxtal	-	0.75	4	n	131
Droxtal-b	Droxtal	-	0.76	6	n	90
Spheres 6	Spheres	-	.94	12	y	60

**Table 3:** Summarize of the results derived from remote sensing and in situ.

‘ $1 \geq Q \geq .7$ ’ corresponds to Plate-c and Compact-b

‘ $Q = .05$ ’ corresponds to Plate-b

‘ $Q \geq 1$ ’ corresponds to Columns, Compacts, CERES-Big and CERES-Nov1

Date July 2002	UT						
	SATELLITES					IN SITU	
						Ratio	Shape
11	Z0	Columns				111	MODIS_rough
	Z1	Columns				116	Columns-B
	Z2	Columns				119	Columns-B
	Z3	Spheres				119	Columns-B
	LIDAR					IN SITU	
		Q<.05 spheres	.05<Q<.7	.7<Q<1.05	Q>1.05	Ratio	Shape
23	1) 19.72-19.74	16%	75 %	7%	2%	117	Columns-B
	2) 19.78-19.82	40	32	8	20	117	Columns-B
	3) 20.23-20.32	14	25	32	29	117	Columns-B
	4) 21.16-21.22	15	20	28	37	117	Columns-B
	5) 21.67-21.75	20	25	25	30	119	Columns-B
	6) 22.16-22.17	12	13	0	75	119	Columns-B
	7) 22.57-22.62	27	25	16	32	119	Columns-B
	8) 23.05-23.20	22	32	25	21	121	Columns-B
26	1) 17.40-17.43	90	10	0	0	121	Columns-B
	2) 18.28-18.51	6	7	68	19	121	Columns-B
	3) 19.01-19.14	2	20	61	17	121	Columns-B
	4) 19.16-19.21	1	7	49	43	121	Columns-B
29	1) 19.88-19.93	23	43	20	14	121	Columns-B
	LIDAR					SATELLITES	
23	Z1	22	59	11	8	Columns	
	Z2	45	44	4	6	Spheres	
29	Z1	36	47	13	4	Plates / BR /MODIS-1 /MODIS-2	

## Figure caption

**Figure 1:** Cloud areas selected for dual satellite retrieval method as seen by GOES-8. The line represents the WB57 flight track. a) 9<sup>th</sup> b) 11<sup>th</sup> of July

**Figure 2:** Cloud areas selected for lidar retrieval, as seen by the CPL onboard the ER-2. The line represents the WB57 flight track. a) 23<sup>th</sup> b) 26<sup>th</sup> c) 29<sup>th</sup> of July.

**Figure 3:** Examples of scattering phase functions.

**Figure 4 :** Dual satellite method. Ratio between Goes-8 and Noaa-16 radiances as a function of Goes-8 radiances. Theoretical computation in line and measurements in dots. a) 9<sup>th</sup> b) 23<sup>th</sup>

**Figure 5:** Lidar method. Histogram of particle shape ratio retrieved along the WB57 aircraft. 23<sup>th</sup> segments 1-8

**Figure 6 :** In situ method. Forward to backscattering ratio as measured by the CAS as a function of time, and theoretical computed ratio (horizontal line).

Figure 1 :

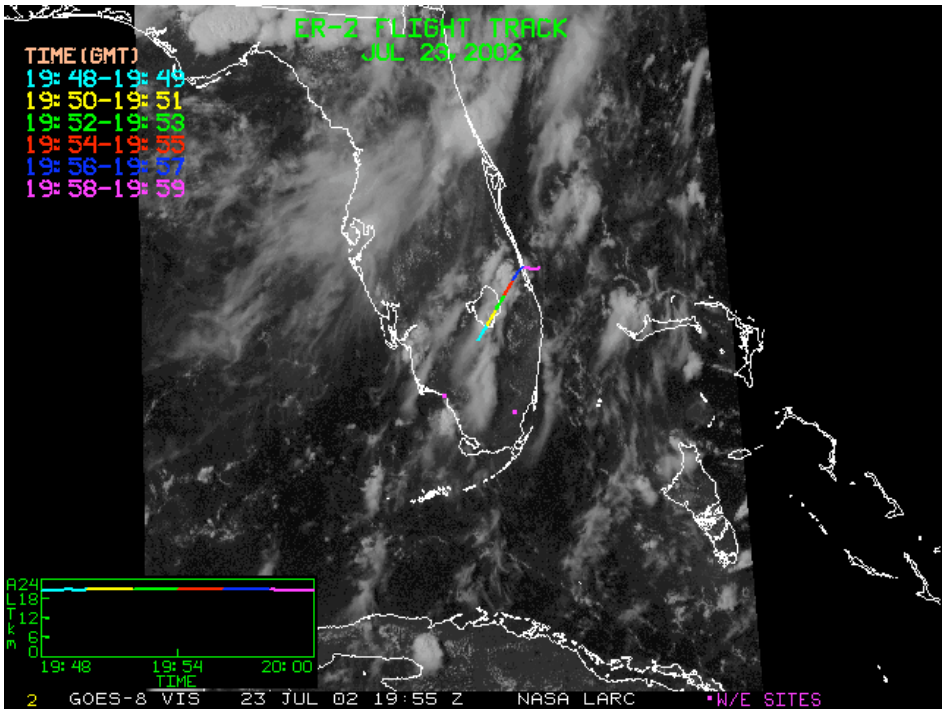
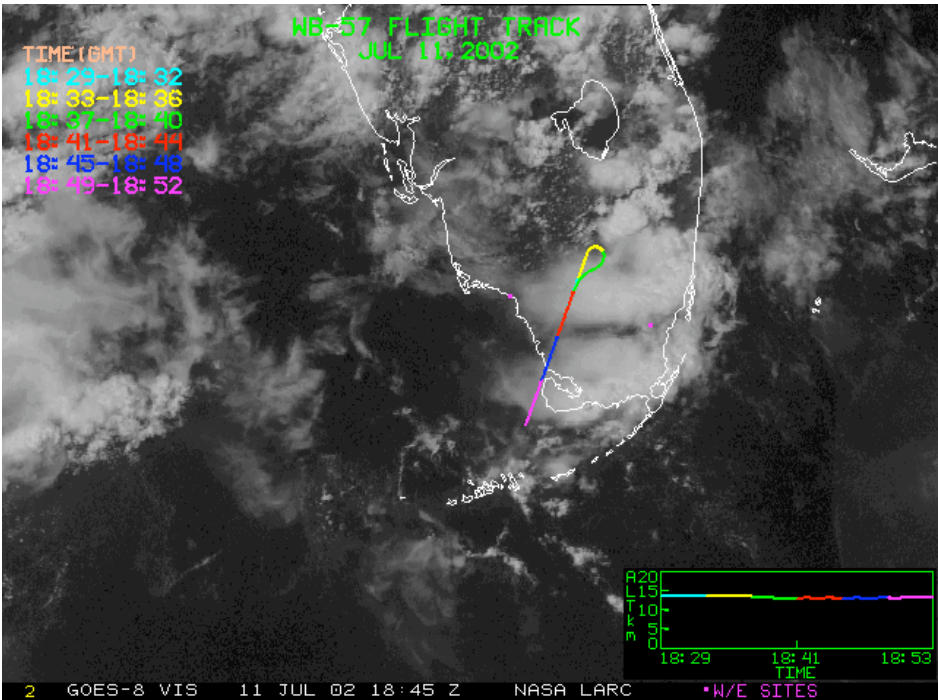
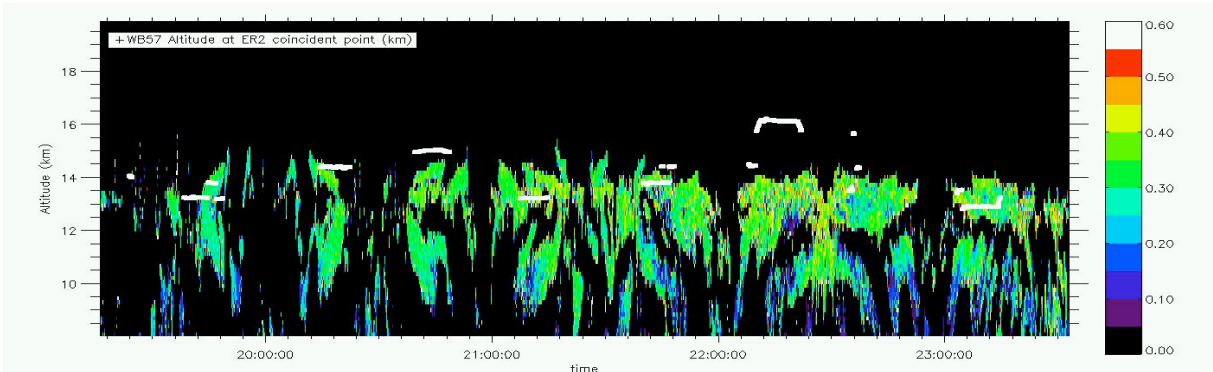
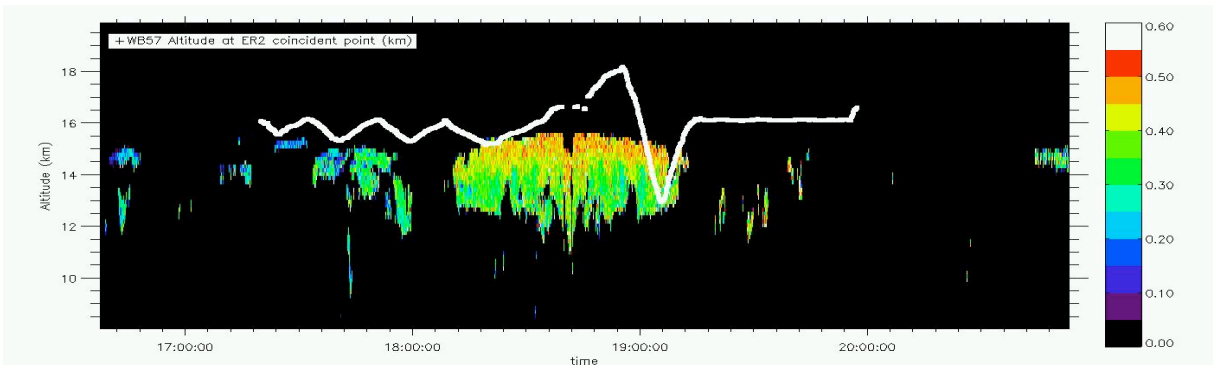


Figure 2:

a) 7/23



b) 7/26



d) 7/29

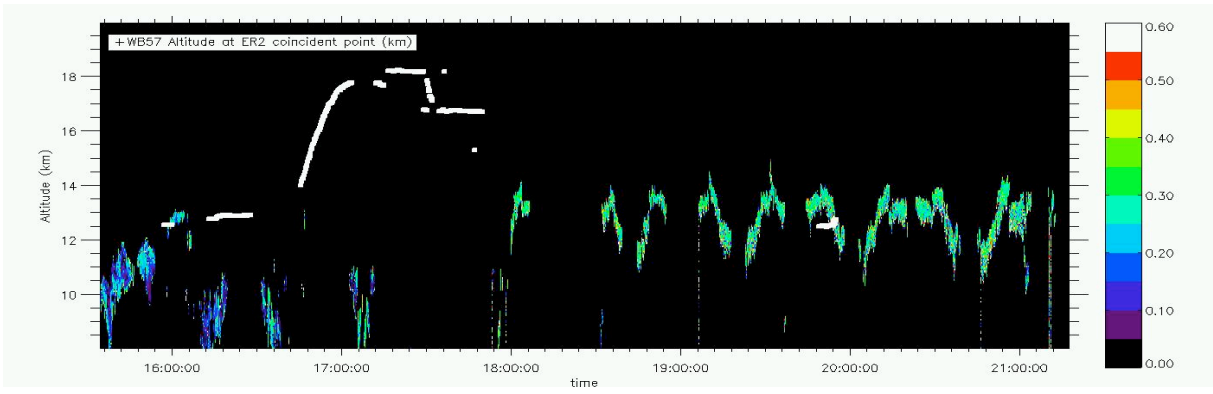
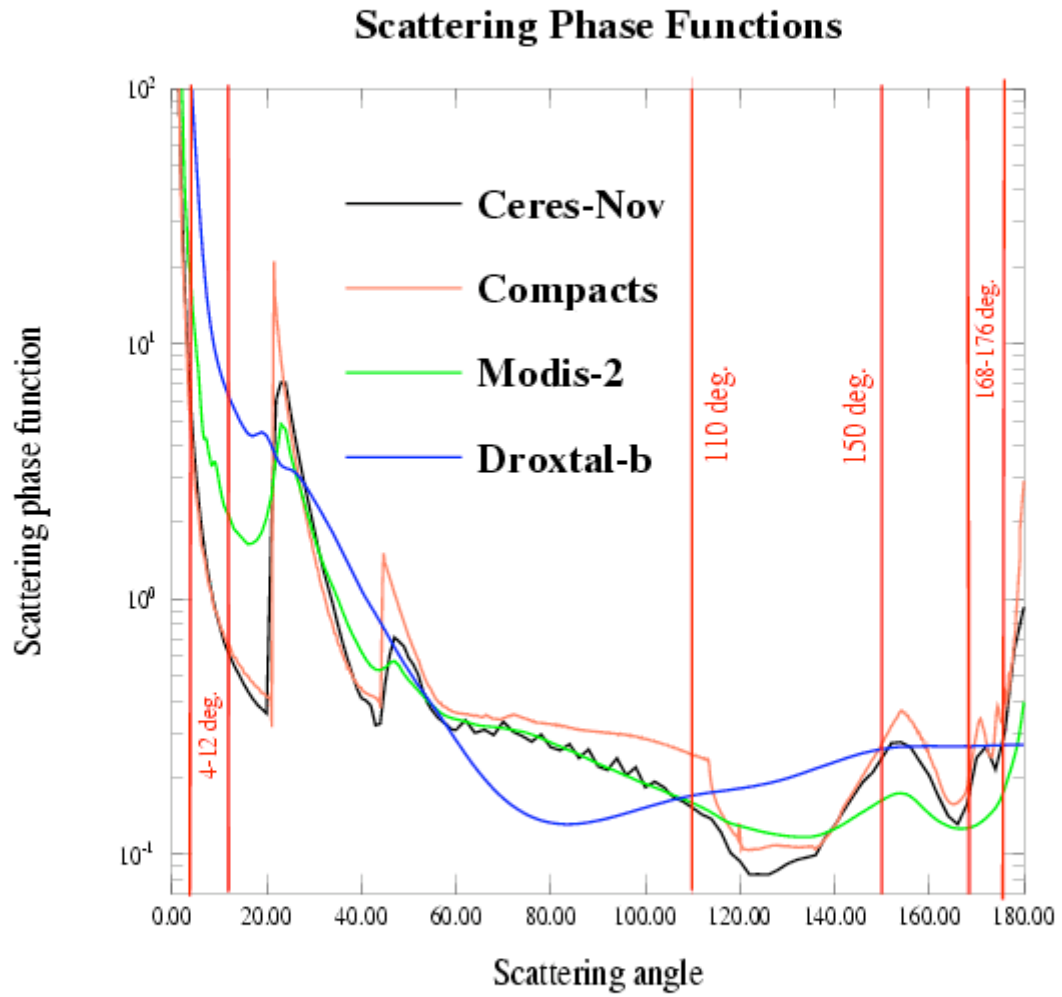


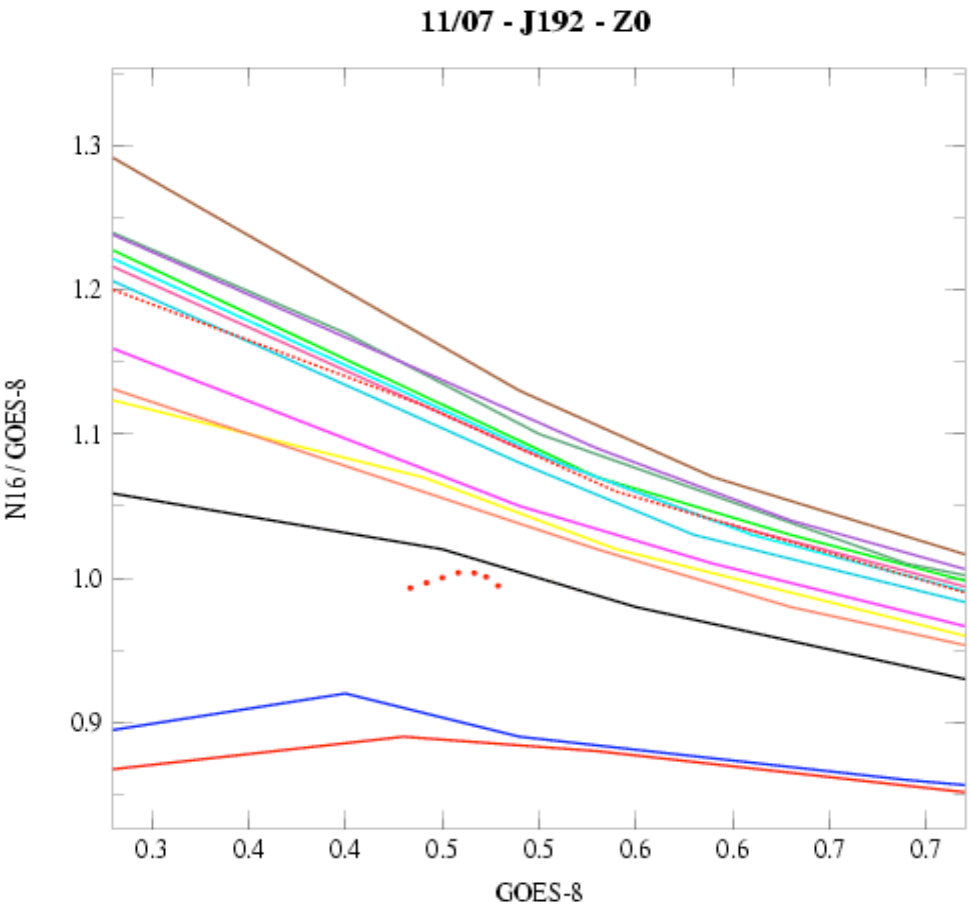
Figure 3:



R11 Sep 3 17:08:02 2004 L.O.A. Computer Team

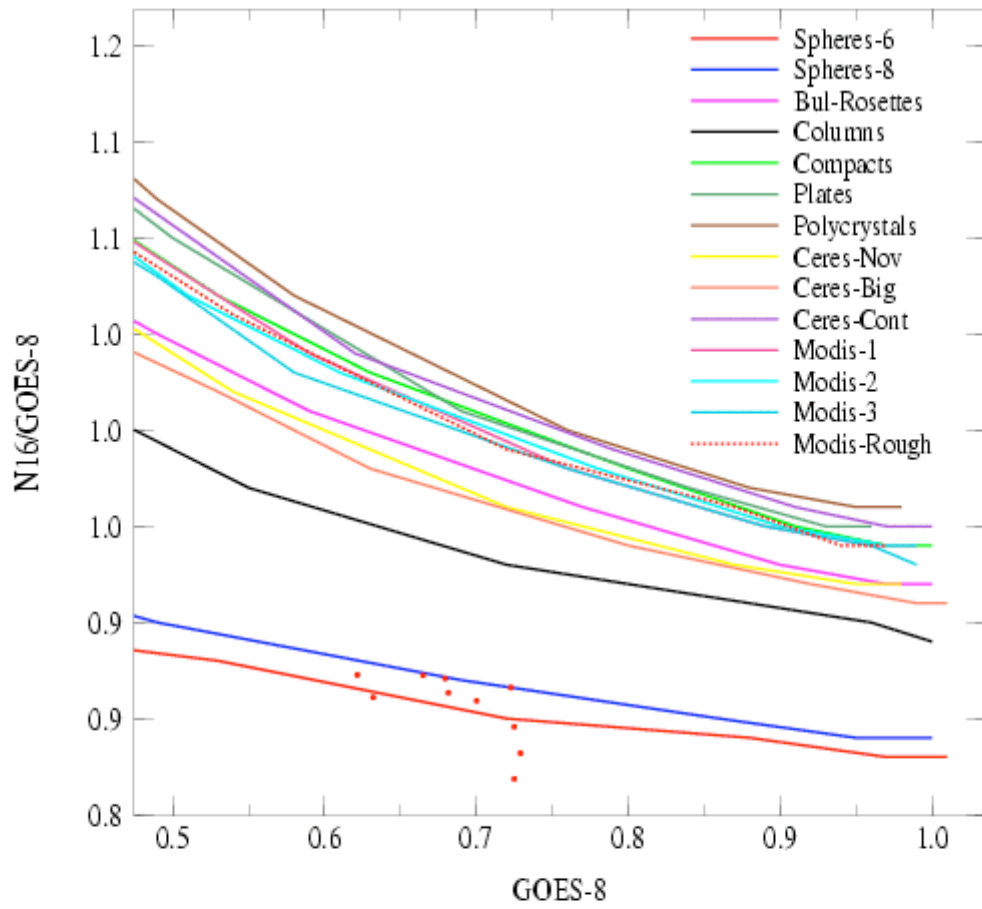


Figure 4 : Dual satellites method.



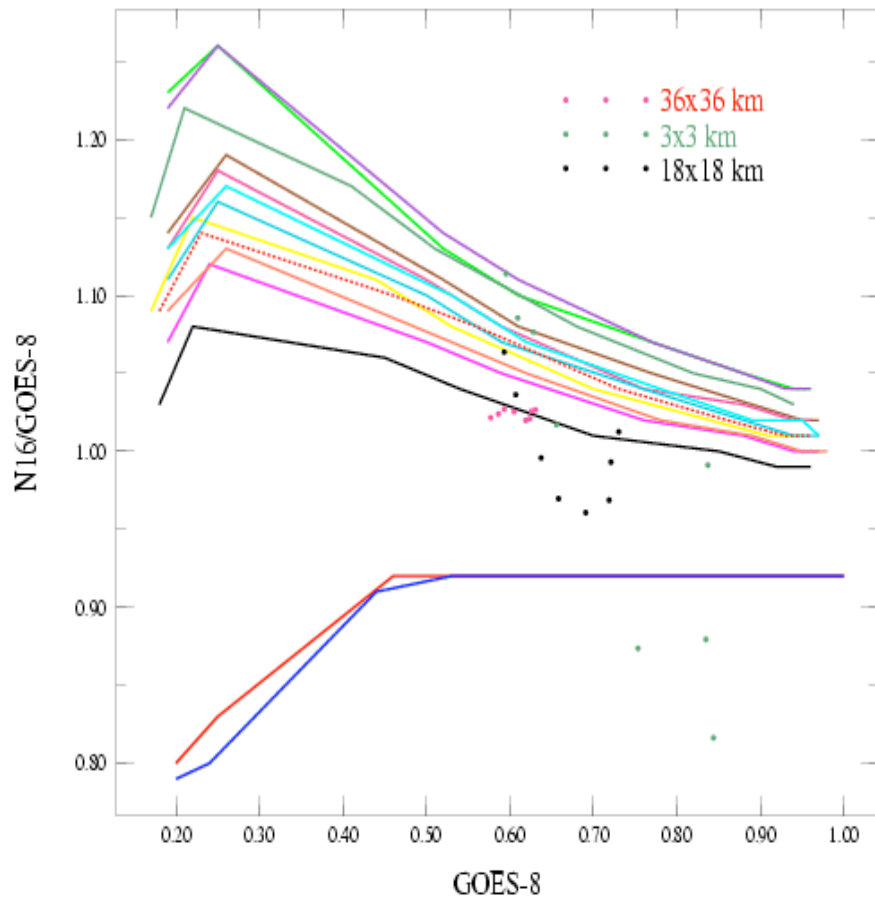
R15 Sep 3 17:28:25 2004 L.O.A. Computer Team

11/07 - J192 - Z3



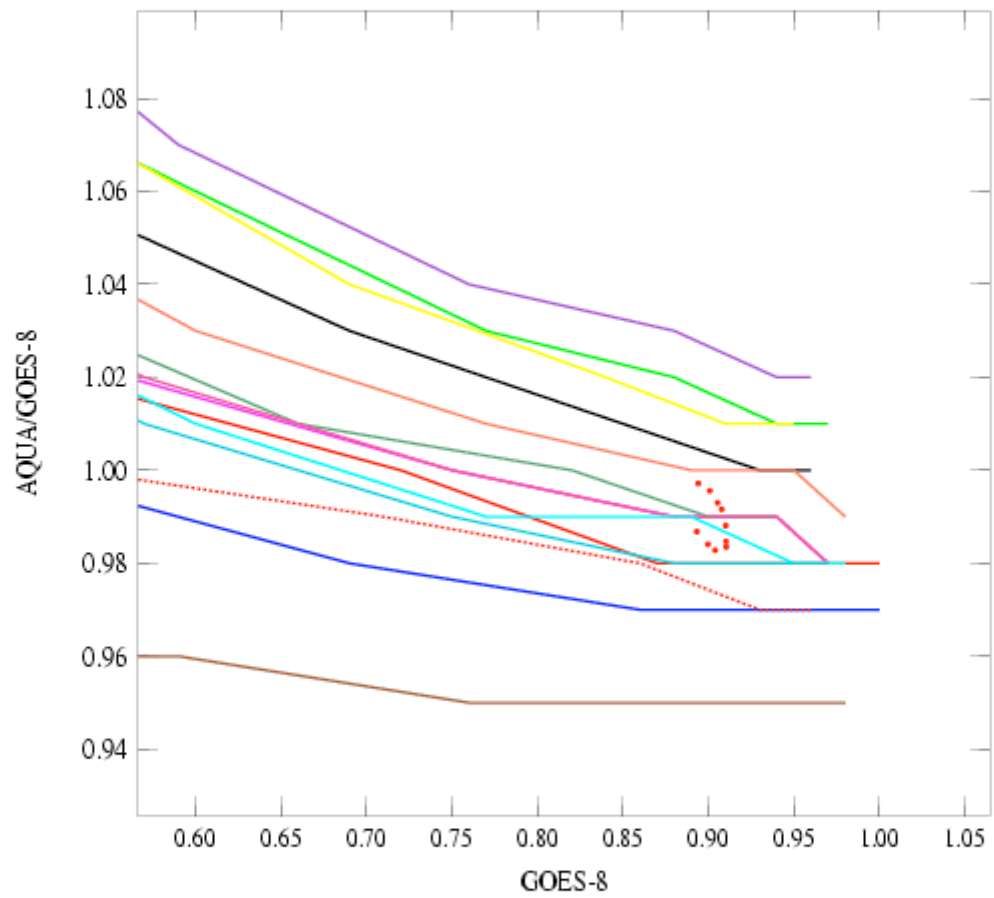
Pl Sep 3 17:23:36 2004 L.O.A. Computer Team

23/07 - J204 - Z1



Tue Jun 15 04:50:15 2004 L.O.A. Computer Team

29/07 - J210



R15 Sep 3 17:34:24 2004 L.O.A. Computer Team

Figure 5 : Lidar retrieval - 7/23

Histogram of each class of shape ratios : class 1 ( $Q < 0.05$ ), class 2 ( $0.05 < Q < 0.7$ ), class 3 ( $0.7 < Q < 1.05$ ), class 4 ( $Q > 1.05$ )

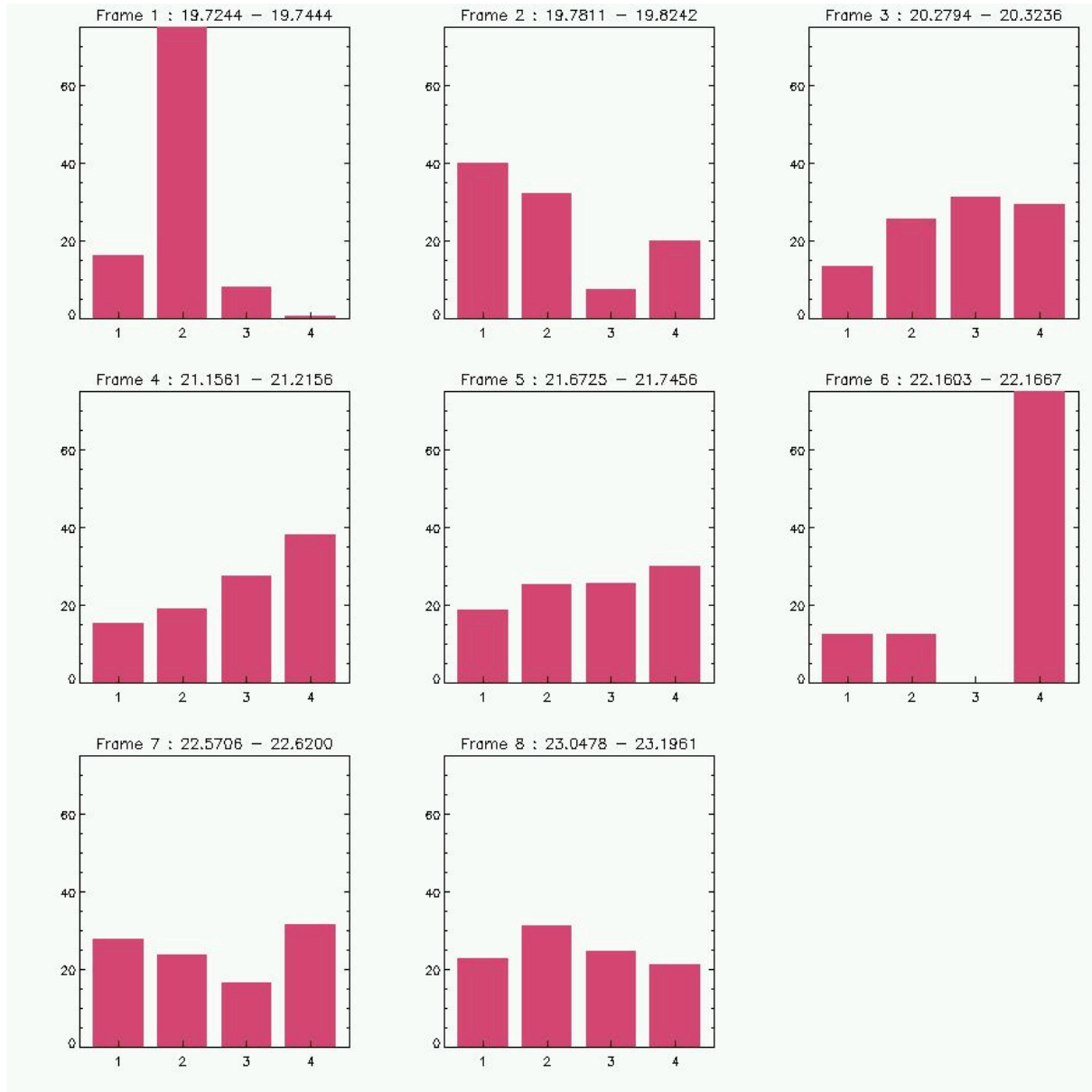
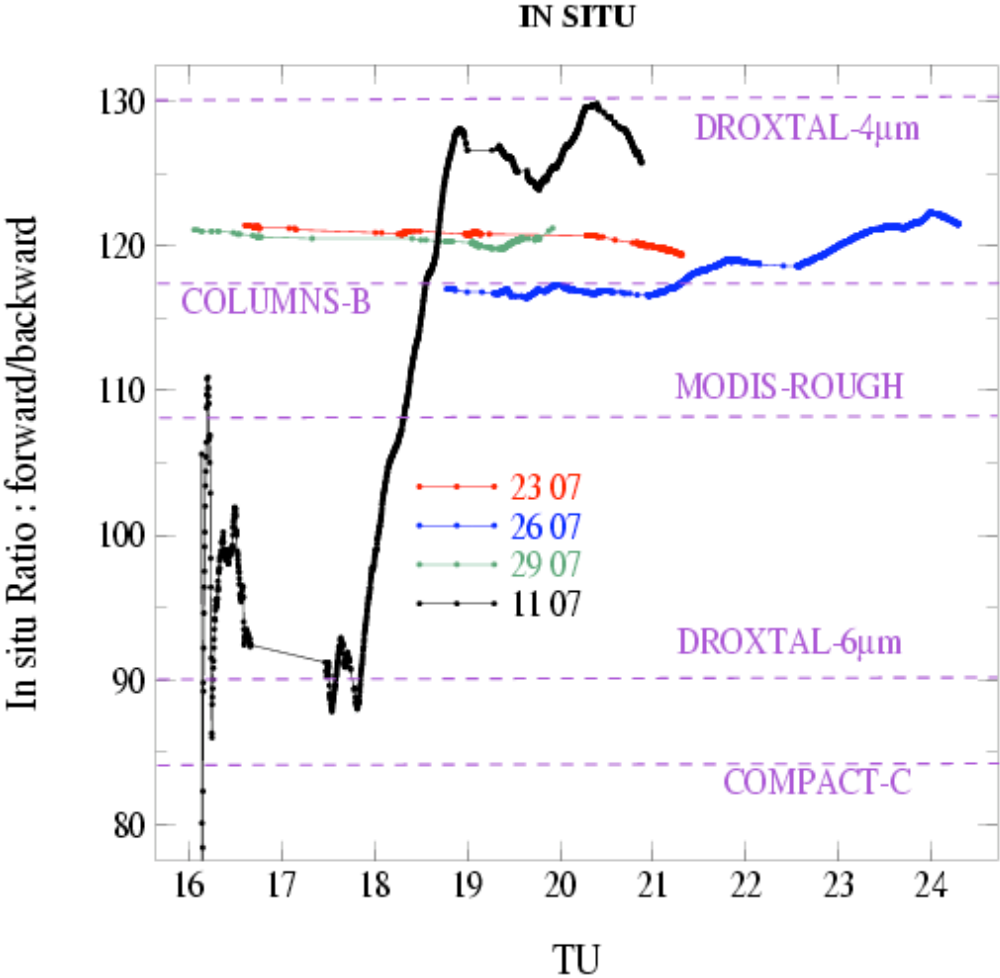


Figure 6 : In situ



Mon Jun 7 15:46:25 2004 L.O.A. Computer Team